Supporting inforamtion for

Construction of Sandwich-like Porous Structure of Graphene-Coated Foam Composites for Ultrasensitive and Flexible Pressure Sensor

Li Zhao[1#], Fei Qiang[1#], Shou-Wei Dai[1], Shi-Chang Shen[1], Yun-Zhuo Huang[1], Neng-Jian Huang[1], Guo-Dong Zhang[1], Li-Zhi Guan[1,2], Jie-Feng Gao[3], Yihu Song[4], Long-Cheng Tang[1*]

[1] Key Laboratory of Organosilicon Chemistry and Material Technology of Ministry of Education, Hangzhou Normal University, Hangzhou 311121, PR China

[2] Instituto de Ciencia de Materiales de Madrid-ICMM, Consejo Superior de Investigaciones Cientificas-CSIC, Campus de Cantoblanco, 28049 Madrid, Spain

[3] School of Chemistry and Chemical Engineering, Yangzhou University, Yangzhou, Jiangsu, 225002, PR China

[4] MOE Key Laboratory of Macromolecular Synthesis and Functionalization, Department of Polymer Science and Engineering, Zhejiang University, Hangzhou 310027, China

[*]Corresponding author. Email: lctang@hznu.edu.cn (L.C.T.)

[#]These authors contributed equally to this work.

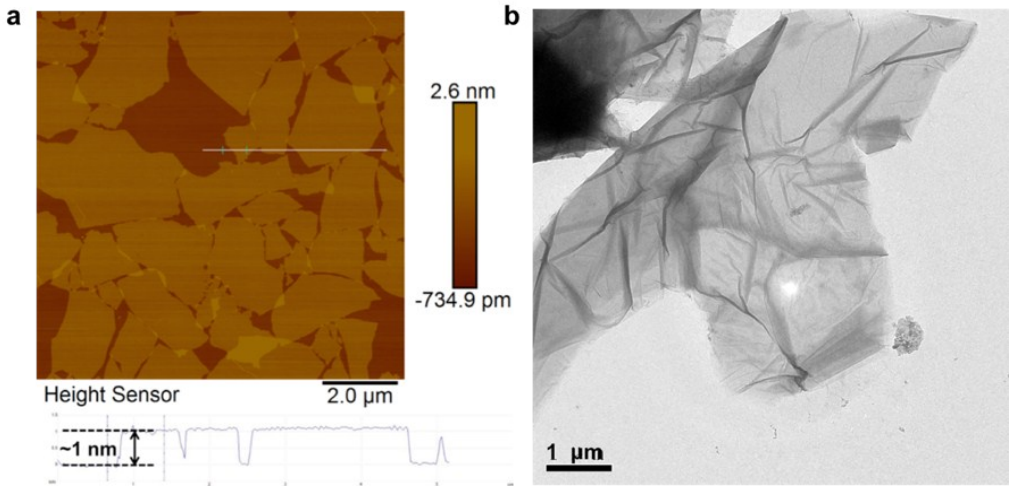

Figure S1. Structure and morphology of GO sheets. (a) A typical AFM image of GO sheets with lateral size ranging from 1-10 µm. The height difference between the steps is ~1.0 nm, indicating the typical height of a single layer GO sheet. (b) TEM image of a typical GO sheet showing wrinkled structures.

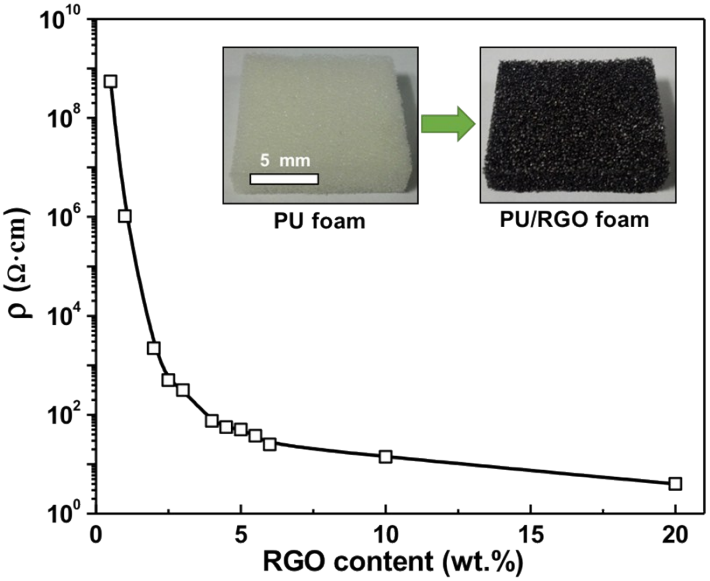

Figure S2. Electrical resistivity changes of the RGO@PU composites. The electrical conductivity of RGO@PU prepared by a facile dip-coating process are strongly dependent on the RGO loading. When the content of RGO is >5 wt%, the electrical resistivity has little change, and the 10 wt% RGO was used in this work to ensure good conductive network of RGO on the foam surface [1]. Insets are digital images of pure PU foam (left) and RGO@PU foam (right).

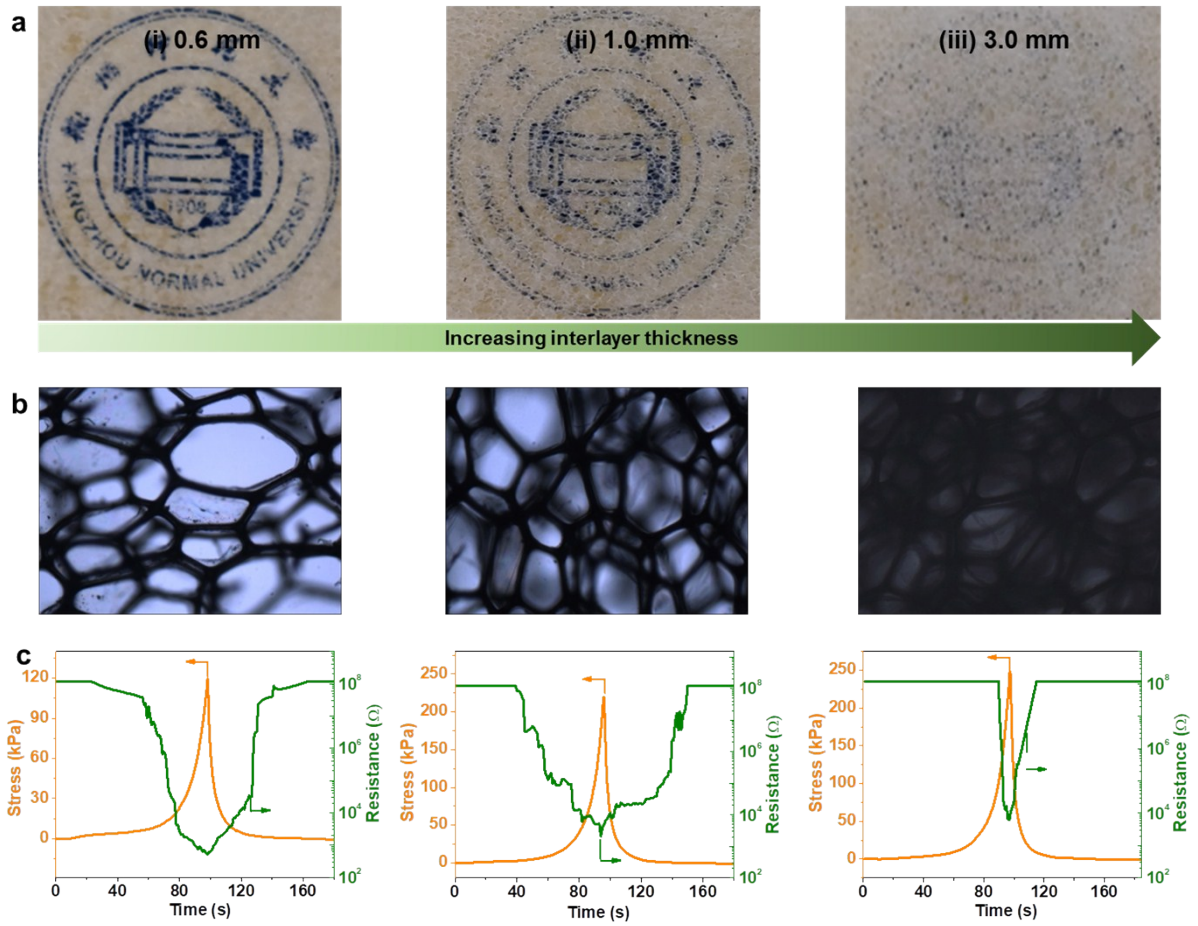

Figure S3. **Structure of porous interlayer at different thickness values and their resistance change of the corresponding SPS sensors:** (a) Photographs of middle layers with different thickness values (0.6, 1.0 and 3.0 mm), showing different light transmittance; (b) TOM images of three middle layers under the same light intensity, suggesting the increased insulating effect with increasing the interlayer thickness; (c) relative electrical resistance response curves of the SPS sensors (ε=80%) for different interlayer thickness values. The thinner interlayer of the SPS sensor produced higher resistance changes under the same pressure and strain conditions.

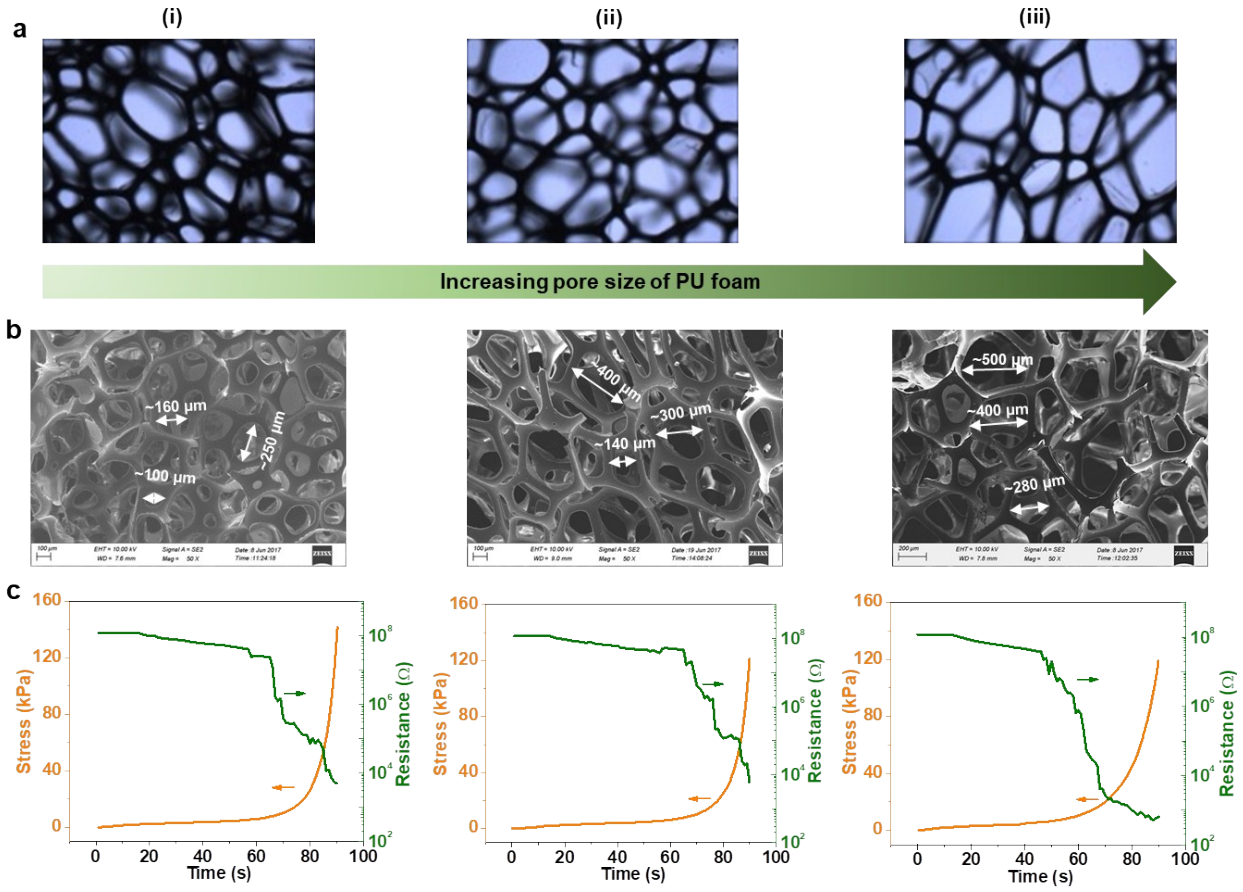

Figure S4. Effect of interlayer microstructure on the resistance response of SPS sensor: (a) TOM images of middle layers with different pore sizes under the same light intensity, showing enhanced interpenetrating effect; and (b) the corresponding SEM images of the middle layers, showing average pore size of 160±45 μm, 270±68 μm, and 368±60 μm (calculated from ~100 pores), respectively, for the above three samples; (c) relative resistance response curves of interlayers SPS sensors with different pore sizes (ε=80%).

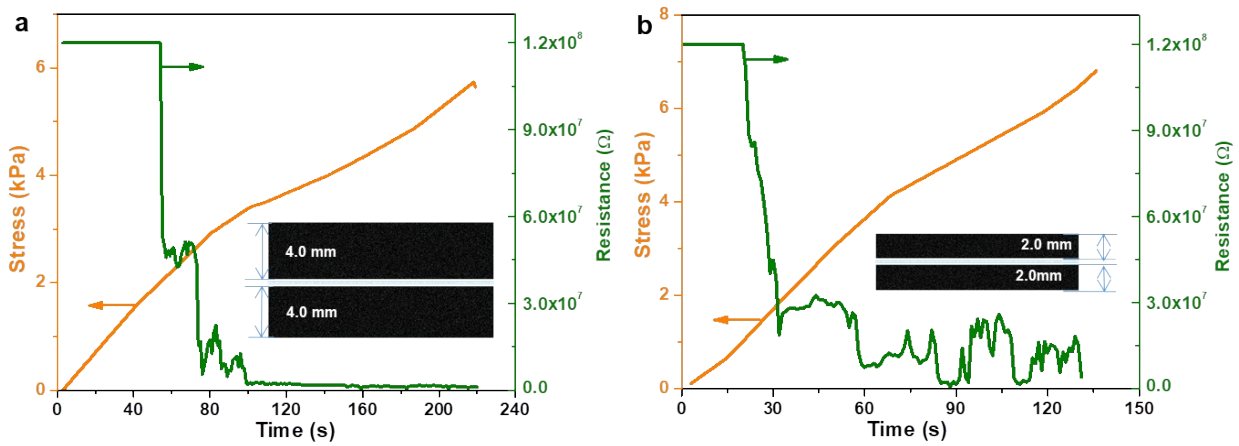

Figure S5. Relative electrical resistance response curves of SPS sensors at different conductive layer thickness: (a) 4.0 and (b) 2.0 mm, showing some differences in response behavior.

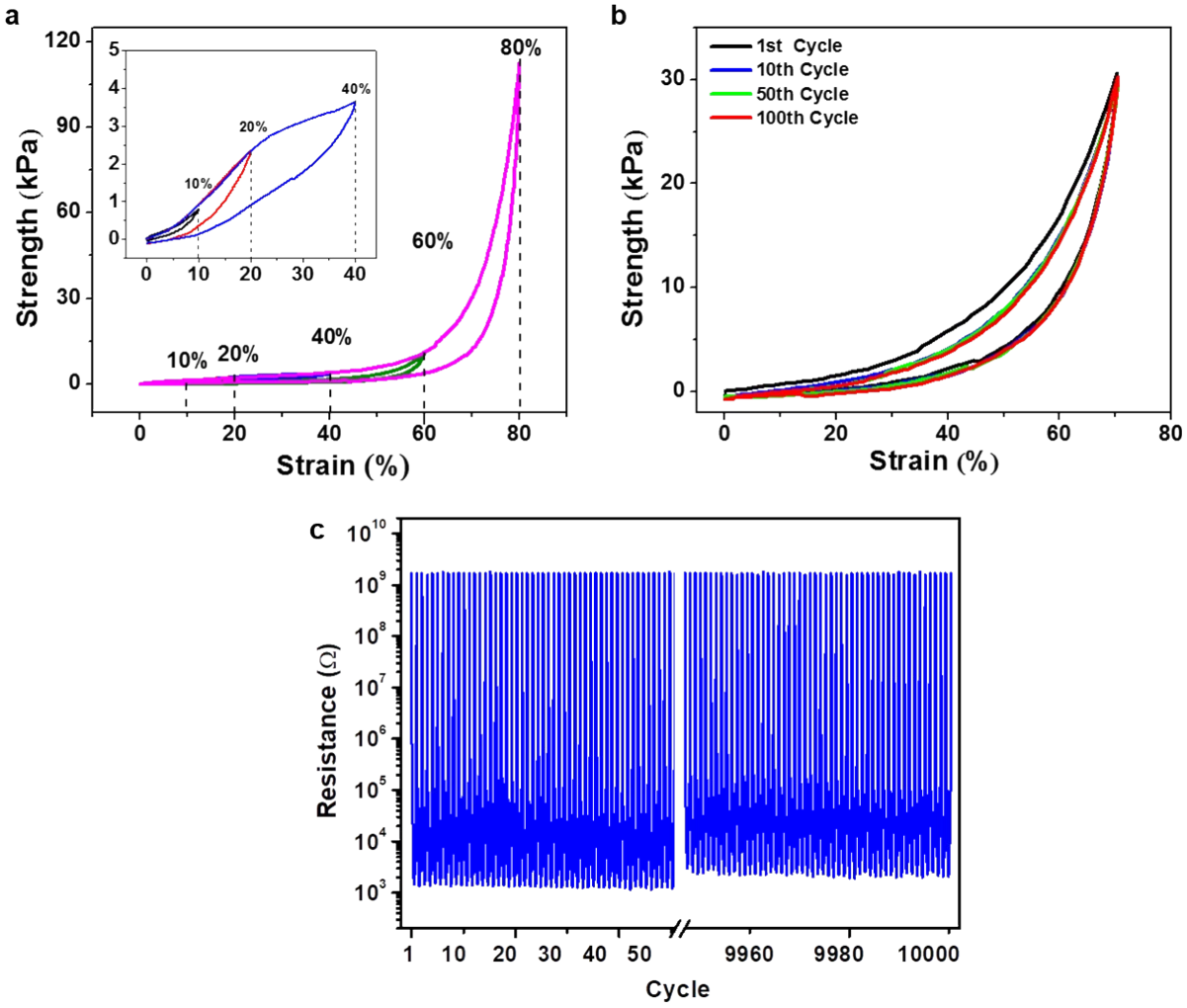

Figure S6. Cyclic compressive properties of the SPS sensors: (a) Typical stress-strain (σ-ε) curves of SPS sensors at different strains (ε=10%, 20%, 40%, 60%, 80%); (b) cyclic compressive test of the SPS sensors at ε=70% strain for 100 cycles; and (c) Resistance change of the SPS sensors during the cyclic compression process. The maximum stress and recovery were almost maintained even after 100 compressive cycles, showing excellent mechanical stability. During 10000 compressive test, the electrical resistance can recover to the original level for each cycle, demonstrating the stability and reliability of the SPS sensor.

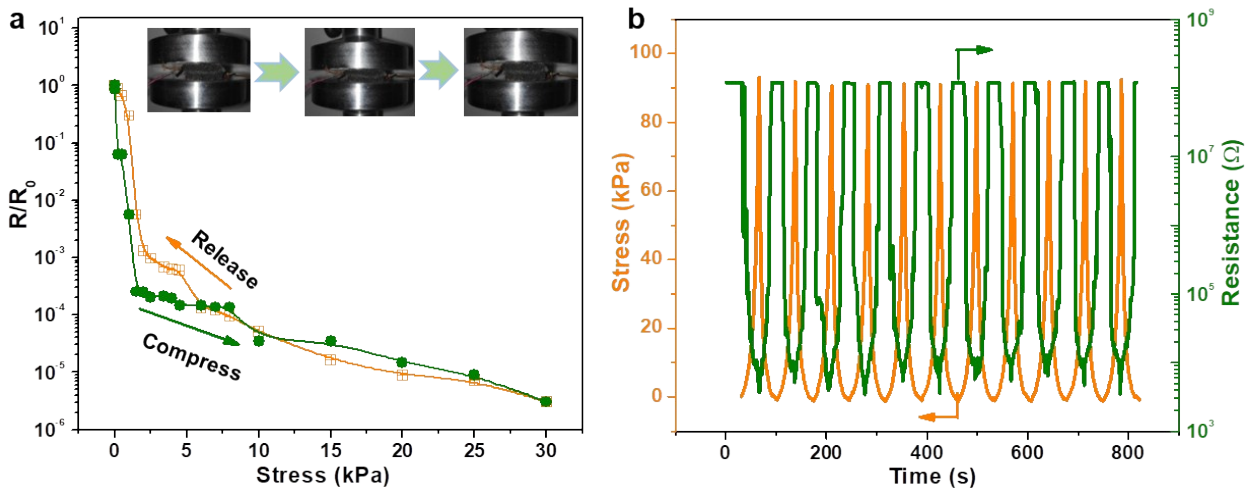

Figure S7. Response stability and correspondence during compression and recovery process: (a) Electrical resistance response of SPS sensors under pressure (0-30 kPa) and release process, excellent response behaviors are manifested in the process of compression and release processes. Inserts are digital photos of the SPS sensor under compressive process. (b) Compressive stress and relative resistance response curves of the SPS sensors, indicating a stable response during the cyclic compression test.

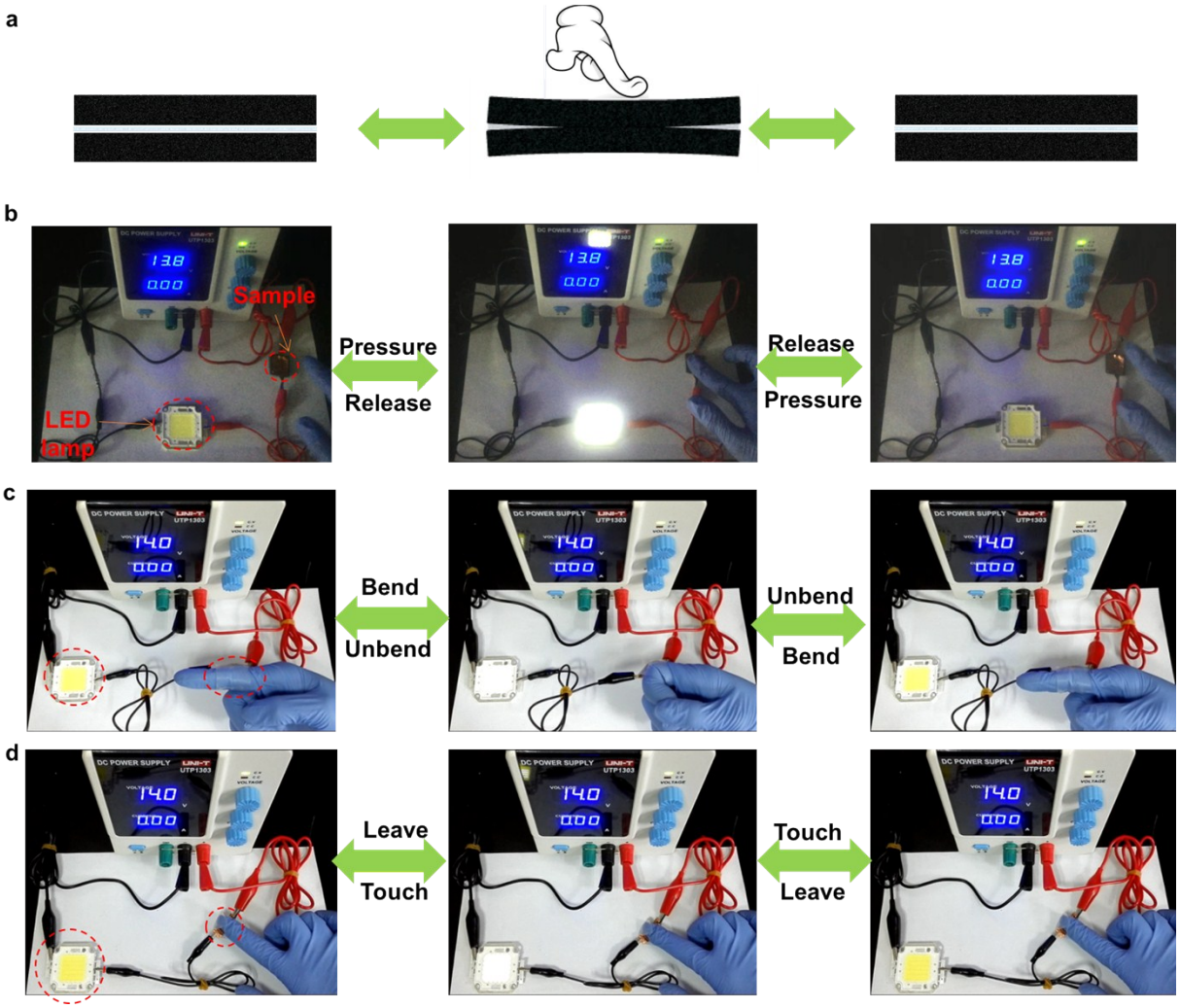

Figure S8. Demo results of the SPS sensors: (a) Schematic illustration of the conductive pathways in the SPS sensors during finger compression; (b-d) photographs of different motion behavior on the as-prepared SPS sensors when connecting the LED: (b) finger compress, (c) finger bend, (d) finger touch.

Table S1. Comparison of the sensitivity and response time of our device with those reported in the literature.

Device type	Sample information	Response time (ms)	Pressure Sensitivity (kPa^{-1})	Reference
Resistive	***SPS of graphene-coated foam***	***10***	***0.67***	***This work***
Capacitance	Pyramid PDMS film on PET	<300	0.55	[2]
Resistive	Graphene coated PU sponge	--	0.26	[3]
Capacitance	Polymer transistors on polyimide	10	8.4	[4]
Resistive	Au-nanowire tissue paper	17	1.14	[5]
Resistive	Microstructured graphene arrays on PDMS film	0.2	5.53	[6]
Resistive	Microsized pyramids array on PDMS	200	4.88	[7]
Capacitance	Ag nanoparticles coated Kevlar fiber	10	0.21	[8]
Capacitance	Carbon nanotube microyarns	63	0.034	[9]
Resistive	Hierarchical graphene/PDMS array	30	14	[10]
Resistive	CNT coated cotton based device	24	14.4	[11]
Piezoresistive	3D graphene/PDMS hollow structure	1.2	15.9	[12]
Piezoresistive	Aligned CNT/graphene/PDMS film	16.7	19.8	[13]
Resistive	Carbonized silk nanofiber membrane	16.7	34.47	[14]
Piezoelectric	Nanowires/graphene heterostructures on PI film	5-7	9.4×10^{-3}	[15]

PDMS: polydimethylsiloxane; PI: polyimide; PET: polyethylene terephthalate.

Reference

1. Q. Wu, L.-X. Gong, Y. Li, C.-F. Cao, L.-C. Tang, L. Wu, L. Zhao, G.-D. Zhang, S.-N. Li, J. Gao, Y. Li and Y.-W. Mai, *ACS Nano*, 2018, **12**, 416.
2. S. C. Mannsfeld, B. C. Tee, R. M. Stoltenberg, C. V. Chen, S. Barman, B. V. Muir, A. N. Sokolov, C. Reese and Z. Bao, *Nat. Mater.*, 2010, **9**, 859.
3. H. B. Yao, J. Ge, C. F. Wang, X. Wang, W. Hu, Z. J. Zheng, Y. Ni and S. H. Yu, *Adv. Mater.*, 2013, **25**, 6692.
4. G. Schwartz, B. C. Tee, J. Mei, A. L. Appleton, D. H. Kim, H. Wang and Z. Bao, *Nat. Commun.*, 2013, **4**, 1859.
5. S. Gong, W. Schwalb, Y. Wang, Y. Chen, Y. Tang, J. Si, B. Shirinzadeh and W. Cheng, *Nat. Commun.*, 2014, **5**, 3132.
6. Z. Bowen, N. Zhiqiang, W. Hong, L. W. Ru, W. Hua, L. Yuangang, Z. Liyan, W. Jun, H. Fengwei and C. Xiaodong, *Small*, 2014, **10**, 3625.
7. C.-L. Choong, M.-B. Shim, B.-S. Lee, S. Jeon, D.-S. Ko, T.-H. Kang, J. Bae, S. H. Lee, K.-E. Byun, J. Im, Y. J. Jeong, C. E. Park, J.-J. Park and U.-I. Chung, *Adv. Mater.*, 2014, **26**, 3451.
8. J. Lee, H. Kwon, J. Seo, S. Shin, J. H. Koo, C. Pang, S. Son, J. H. Kim, Y. H. Jang, D. E. Kim and T. Lee, *Adv. Mater.*, 2015, **27**, 2433.
9. S. Y. Kim, S. Park, H. W. Park, D. H. Park, Y. Jeong and D. H. Kim, *Adv. Mater.*, 2015, **27**, 4178.
10. G. Y. Bae, S. W. Pak, D. Kim, G. Lee, D. H. Kim, Y. Chung and K. Cho, *Adv. Mater.*, 2016, **28**, 5300.
11. M. Liu, X. Pu, C. Jiang, T. Liu, X. Huang, L. Chen, C. Du, J. Sun, W. Hu and Z. L. Wang, *Adv. Mater.*, 2017, **29**, 1703700.
12. N. Luo, Y. Huang, J. Liu, S.-C. Chen, C. P. Wong and N. Zhao, *Adv. Mater.*, 2017, **29**, 1702675.
13. M. Jian, K. Xia, Q. Wang, Z. Yin, H. Wang, C. Wang, H. Xie, M. Zhang and Y. Zhang, *Adv. Funct. Mater.*, 2017, **27**, 1606066.
14. Q. Wang, M. Jian, C. Wang and Y. Zhang, *Adv. Funct. Mater.*, 2017, **27**, 1605657.
15. Z. Chen, Z. Wang, X. Li, Y. Lin, N. Luo, M. Long, N. Zhao and J. B. Xu, *ACS. Nano.*, 2017, **11**, 4507.